Applied Catalysis B: Environmental 336 (2023) 122952

Contents lists available at ScienceDirect

Applied Catalysis B: Environmental

journal homepage: www.elsevier.com/locate/apcatb

Why is calcium an effective promoter for plasma CO_2 methanation over polymer P123-modified NiMgAlOx-mixed oxide catalysts?

Minh Nguyen-Quang [a,b,c], Federico Azzolina-Jury [a,*], Bogdan Samojeden [b], Monika Motak [b,*], Patrick Da Costa [c]

[a] Laboratoire Catalyse et Spectrochimie (LCS), CNRS-ENSICAEN-Université de Caen, 6 boulevard du Maréchal-Juin, 14000 , France
[b] Faculty of Energy and Fuels, AGH University of Science and Technology, Al. Mickiewicza 30, 30-059 Kraków, Poland
[c] Institut Jean le Rond d'Alembert, Sorbonne Université, CNRS UMR 7190, 2 place de la gare de ceinture, 78210 Saint Cyr l'Ecole, France

ARTICLE INFO

Keywords:
3P-NMA
Ca-Ba promoters
hydrotalcite, DBD-assisted CO_2 methanation,
conventional CO_2 conversion

ABSTRACT

This work demonstrated the impact of Ca and Ba on the properties and activity of Polymer P123-modified NiMgAlOx-mixed oxide catalysts over thermal and plasma CO_2 methanation. Both elements influenced the basicity and redox properties of the 3 P-NMA catalyst. Although the high CO_2 affinity of the promoted-Ca catalyst limited its low-temperature performance, the plasma tests revealed efficient conversion of carbonates to methane, attributed to the presence of highly energetic electrons. Ni15Ba1 demonstrated notable effectiveness in conventional tests (X_{CO_2} = 80.5%, S_{CH_4} = 99.7%, at 250ºC), meanwhile, Ni15Ca1 displayed a significant enhancement in plasma (X_{CO_2} = 86.8%, $S_{CH_4} \approx$ 100%, at 24.8 W discharge power), with 73.5% of energy efficiency, the highest reported. Both catalysts showed increased conversion to 88–89% at 300ºC. *Operando* FTIR measurements uncovered the different intermediates under thermal and plasma conditions. The Ca concentration was optimized at 1 wt% for plasma performance, likely due to the strong adsorption capacity of Ca and the catalyst dielectric constant.

1. Introduction

The utilization of fossil fuels has a detrimental impact on the biosphere and has led to significant concern about global climate change caused by the emission of greenhouse gases, with carbon dioxide being the primary contributor. Studies estimated that if the current concentration of CO_2 were to double pre-industrial levels, there would be a 1.5°− 4.5 °C (2.7°−8.1°F) increase in global average surface temperatures, current concentrations are approximately 1.4 times pre-industrial levels [1]. In the last years, CO_2 capture and utilization (CCU) has gained significant attention [2,3] as a means to mitigate the harmful effects of greenhouse gases. By utilizing CO_2 as an alternative to geological storage, not only CO_2 emissions can be reduced to combat global climate change, but it also presents the opportunity to produce various value-added feedstock chemicals (e.g., CH_3OH, HCOOH) and fuels (e.g., CH_4, C_2H_4) to meet increasing energy needs and address environmental concerns through sustainable methods.

The process, known as CO_2 methanation or the Sabatier reaction (Eq. 1), uses concentrated CO_2 from industrial sources and H_2 generated by renewable energy-powered water electrolysis to produce CH_4 that can be easily added to existing natural gas transportation systems [4,5].

$$CO_2 + 4\ H_2 = CH_4 + 2\ H_2O,\ \Delta H = -165\ kJ{\cdot}mol^{-1} \quad (1)$$

Between 200 °C and 550 °C, catalytic CO_2 methanation is significantly exothermic and thermodynamically advantageous [6]. Thermal runaway is, therefore, likely to result in thermodynamic restriction and catalyst sintering.

Extensive research has been subjected to develop highly catalytic activity, particularly in the low-temperature range (100–250ºC). Despite the fact that Rh and Ru-based catalysts show high activity at low temperatures and good stability [7], Ni-based catalysts remain the most popular due to their high activity, low cost, and high natural abundance, especially when it comes to industrial scale. Yet, Ni-based catalysts have several downsides, including low-temperature activity compared to Rh- and Ru-based catalysts, as well as Ni nanoparticle sintering and coke formation. These limitations can be easily overcome through the incorporation of a metal or metal oxide promoter [7,8].

Apart from some well-known elements, such as transition, noble

* Corresponding authors.
E-mail addresses: federico.azzolina-jury@ensicaen.fr (F. Azzolina-Jury), motakm@agh.edu.pl (M. Motak).

https://doi.org/10.1016/j.apcatb.2023.122952
Received 13 March 2023; Received in revised form 31 May 2023; Accepted 1 June 2023
Available online 1 June 2023

metals, the incorporation of alkali and, particularly, alkaline earth metals, such as Ca and Ba, as promoters has been already proposed but less studied. These metals are abundant and cost-effective. They have the potential to promote CO_2 methanation by increasing support basicity and introducing oxygen vacancies, thereby favoring the initial CO_2 chemisorption or by strongly modifying the work function and, thus, the properties of the active metal phase [9–11].

Liu et al. [10] conducted a comprehensive study in which a range of alkaline earth metals (Mg, Ca, Ba, Sr) was doped on Ni/CeO_2 catalysts. During the citrate sol-gel synthesis, alkaline earth metal nitrates were introduced at a molar ratio of 1–9 with respect to $Ce(NO_3)_3.6\ H_2O$. Mg^{2+} and Ca^{2+} appeared to dissolve entirely into the CeO_2 lattice, whereas the other two samples had secondary phases of $SrCO_3$ and $BaCO_3$. At low temperatures, the Ca-doped catalyst produced the highest CO_2 conversion and increased turnover frequency (TOF), while the Sr-doped catalyst was second-best. Guo et al. [12] investigated the influence of Ba and Ca on CO_2 methanation over Ni/SiO_2 catalysts. Under the reaction conditions (WHSV = 15,000 ml.$(g_{cat.}h)^{-1}$, $H_2/CO_2 = 4$, P = 1 atm, and 350 °C), the scientists discovered that the addition of BaO enhanced the CO_2 conversions to 67.6%, compared to 64.7%. In the meantime, CH_4 selectivities remained above 98%. According to the authors, CaO did not have a significant effect.

As structural enhancements, the use of CaO and BaO can enhance the surface basicity of the catalyst. Furthermore, Ba-promoted catalysts may reduce CO generation by inhibiting the reverse water-gas-shift reaction [13]. It is assumed that as a basic modification, CaO can increase CO_2 chemisorption and decrease its activation energy, as reported in [14]. Additionally, Feng et al. [15] found that the addition of CaO increased the amount and the strength of basic sites over a 15Ni/activated carbon (AC) catalyst, thus improving catalytic performance. Moreover, research reported by Xu et al. [16] discovered that Ca might increase the wall thickness of the mesoporous channels of the catalyst, thereby enhancing the thermal stability of the catalysts. Ca promoters also aid in the reduction of Ni species by preventing the formation of $NiAl_2O_4$ spinel in an ordered mesoporous alumina matrix while having no effect on the chemical coordination of Ni^{2+}. Liang et al. [17] observed that 5% Ca doping on Ni/Al_2O_3 resulted in a slight increase in support alkalinity but did not appear to enhance methanation activity.

In summary, previous research focused on the screening of various alkaline earth metals as dopants in CO_2 methanation has yielded inconsistent results, some studies indicating an increase in activity and while others pointing out a decrease (specifically for Mg and Ca). It is important to note that these studies differ in terms of the type of support used, the loading of the alkaline earth metal, and the preparation technique. Therefore, comprehensive studies on the influences of these elements over different catalyst systems still need to be dedicated further. On the other hand, while hydrotalcite-induced mixed-oxide catalyst (HiMO) shows promise [14,18,19], it has received less attention in research endeavors. The development of this type of catalyst remains an open avenue for exploration.

Given the continuous development of the CO_2 methanation process, the applications of new system configurations are widely growing. These last years, research was carried out in order to enhance CO_2 methanation under mild conditions by using non-thermal plasma (NTP). One specific type of NTP, called dielectric barrier discharge (DBD), can activate catalysts by creating energetic electrons and excited species without heating the gas molecules. The use of dielectric barrier discharge (DBD) technology allows for CO_2 methanation to operate at considerably lower temperatures, resulting in reduced energy costs due to lower heat loss [20]. Moreover, it enhances CO_2 conversion and CH_4 selectivity [21,22], stabilizes Ni-based catalysts, improves dispersion [23], and promotes metal-support interactions [24]. These benefits have a huge potential to enhance the performance of catalytic CO_2 methanation [25–28].

Unfortunately, there is a lack of information pertaining to the efficiency of Ca and Ba-promoted HiMO catalyst both under thermal and DBD plasma conditions. This work, therefore, aims to modify HiMO catalysts with a structure-directing agent (polymer P123) and alkaline elements (Ca, Ba) in one-step synthesis. In the sense of implying P123 during the synthesis, our previous research has provided empirical evidence that the introduction of P123 induces significant modifications in the physicochemical properties, morphology, and texture of the original Ni(Mg,Al)Ox (NMA) catalyst while retaining the intrinsic properties of HiMO [29]. We note that the addition of P123 to the synthesis process results in alterations to the coprecipitation pathway. Unlike promoters, which remain on the catalyst and participate in the reaction, P123 is subsequently removed through thermal treatment leaving changes to catalyst structure.

In light of previous studies, the present study aims to provide a detailed clarification on how the incorporation of Ba and Ca to P123-modified NMA impacts the thermal and plasma CO_2 methanation manners. Additionally, this study, completed with thermal and plasma *Operando* FTIR, will advance our understanding of the different intermediates that govern the catalytic activity of Ba and Ca. The results of this study place a primary emphasis on the electrical and plasma consequences of low-temperature activity and provide valuable insights that can inform future research endeavors.

2. Experimental

2.1. Strategy for catalyst synthesis

The investigated catalysts were prepared by co-precipitating cations in a basic solution at 65 °C, as previously described [30]. Acetate salt of Ni and Nitrate salts of Mg, Al, Ca, and Ba as precursors were used to synthesize the catalysts. The amounts were calculated to obtain 15 wt% Ni, 1 wt% Ca, and 1 wt% Ba, with $\frac{\sum(M_i^{3+})}{\sum(M_i^{2+}+M_i^{3+})} = 0.25$, i = cations. Catalysts with varying Ca concentrations (0.5 wt%, 2 wt%, 3 wt%, and 5 wt% Ca) and catalysts without Ni were also synthesized for further study using the same technique. Polymer P123, plays the role of structure-directing agent, was employed during the synthesis step to reinforce the catalyst-layered structure at a concentration of 3 wt%. The self-assembly of P123 in the medium would produce a spatial template [31], which served as a framework for the subsequent coprecipitation of cations. This process led to the modification of the catalyst structure and alterations in its characteristics. The catalysts were then calcined at 550 °C for 5 h with a heating ramp of 2 °C per minute. After the thermal treatment step, hydrotalcite was converted to mixed oxides and P123 was removed, leaving the desired structure to mixed oxide catalysts.

The catalysts were designated by the symbols Ni15Ba1, Ni15Cax (x = 0.5, 1, 2, 3, 5) and Ni0Ca1, while the parent catalyst was named 3 P-NMA. For comparative study, Ni(15 wt%)/$Ce_xZr_{1-x}O_2$ mixed oxides (x = 0.58, Solvay), denoted Ni15/CZ, was synthesized following [32]. The characterization and catalytic tests can be found in [32].

2.2. Physical and chemical characteristics of catalysts

All catalysts were characterized using Inductively Coupled Plasma (ICP), Scanning Electron Microscopy (SEM), low-temperature nitrogen sorption, X-Ray Diffraction (XRD), H_2-Temperature-programmed reduction (H_2-TPR), and CO_2-Temperature-programmed desorption (CO_2-TPD) and FTIR techniques. The dielectric constant of catalysts was also measured. Details of characterizations are available in *Supplementary Notes.*

Operando FTIR experiments were carried out in separate systems for thermal and plasma configurations. For both cases, catalysts were reduced and pressed into self-supported wafers (D = 20 mm, 20 mg).

Note that the DBD-*Operando* FTIR study is still in a very early stage; up until now, there have been only three publications dedicated to such measurements. The first group investigated the C_2H_4/Ar dissociation in DBD plasma [33], and the second paper belonged to our group by investigating isopropanol (IPA) over -Al_2O_3 catalyst [34]. And lastly, the

CO_2 hydrogenation in DBD plasma and in the presence of CuO/ZnO/Al_2O_3 aimed at methanol production [35]. Therefore, this part is critical in terms of contributing to the understanding of the intermediate species formed on the surface of mixed-oxide derived from hydrotalcite catalyst under thermal and DBD-plasma CO_2 methanation. Fig. 1 presents the *Operando* cell.

This *Operando*-DBD configuration allows monitoring the evolution of all bands that appeared on the surface of the catalyst wafer as well as the appearance of species in the gas phase. Sample holder in the sieve shape, which allows the IR beams to pass through and at the same time generate plasma as it plays the role of high voltage electrode.

Spectra and plasma properties were monitored during ca. 20 min to make sure the signals reached the stable stage. FTIR spectra, recorded within 4000–400 cm^{-1} range, were treated in OMNIC™ software. Details of *Operando* setup and protocols are available in *Supplementary Operando FTIR measurements*.

2.3. Methanation of carbon dioxide

Thermal methanation (TM) is composed of a U-shaped quartz reactor coupled to an external K-type thermocouple for temperature monitoring. The catalyst was packed between two layers of quartz wool in the reactor gourd (10 mm I.D.) [30]. The reactant streams were regulated using three mass flow controllers.

For plasma methanation (PM), the DBD plasma reactor consisted of a cylindrical quartz tube (10 mm O.D. 7.6 mm I.D.), an external copper ring (thickness = 8 mm and height = 6 mm) - the ground electrode, and an inner tungsten rod (2 mm O.D.) serving as the high voltage electrode. The tungsten rod was coated with a thin layer (3 mm O.D.) of dielectric alumina, resulting in the double dielectric barrier discharge configuration. The ground electrode was connected in series with a 3.3 pF capacitor. Electrodes were powered by a high voltage alternating current (AC) power source (Minipuls 6) with an input voltage of up to 29 kV and a frequency of up to 70 kHz. Two voltage probes were used to record the electrical signals applied voltage (U_A) and the voltage across the capacitor (U_C) using a digital Pico oscilloscope (PicoScope® 5000 Series) (1000X and 10X for U_A and U_C, respectively). The experiments were done under pseudoadiabatic conditions, in which the plasma reactor was neither thermally insulated nor externally heated. Consequently, the discharge length and the gap of the DBD reactor were 6 mm and 2.3 mm, respectively. The details of the system setup for thermal and plasma tests can be found in the *Supplementary catalytic system setup*.

The mass of the catalyst was determined based on its own density in order to achieve Gas Hourly Space Velocity (GHSV) = 12,000 h^{-1}. All tests were performed under ambient pressure. Prior to methanation, all catalysts were first reduced in-situ at 900 °C for one hour at a flow rate of 100 ml.min^{-1} in a 5% volume/volume combination of H_2 and Ar. A total flow of 100 ml.min^{-1} with H_2/CO_2 = 4/1 was applied for the catalytic tests.

The TM was evaluated at intervals of 50 °C between 250 °C and 450 °C, with the steady state being maintained for 30 min at each temperature. For PM tests, the reaction was conducted at a frequency of f = 12.3 kHz, while the applied peak-to-peak voltage (U_A) was adjusted between 22, 23, and 24 kV, with each condition held for 30 min. All catalysts were re-reduced in plasma (F = 100 ml.min^{-1}, H_2/Ar flow, f = 12.3 kHz, U_A = 24 kV) before the reaction.

The outflow, after passing through a water trap, was analyzed by a micro gas chromatograph (490Varian Micro-GC coupling with two columns, a 5 m PoraBOND Q (PBQ)+ 10 m Molsieve 5 Å (MS 5 A) and a 10 m PoraPlot U (PPU) for Channel 1 and 2, respectively, using He as carrier gas) equipped with Thermal Conductivity Detector (TCD).

The reactions were evaluated in terms of catalytic activity (CO_2 conversion, CH_4 selectivity), discharge power (P, using the Lissajous method [36–39]), and plasma characteristics (Specific energy input, energy efficiency, and energy cost [40,41]). Thermodynamic equilibrium calculation was simulated by the HSC Chemistry 5.0 software using the Gibbs free energy minimization method concerning the working conditions (GHSV = 12,000 h^{-1}, H_2/CO_2 = 4). Further details are presented in *Supplementary Reaction evaluations and diagnostics*.

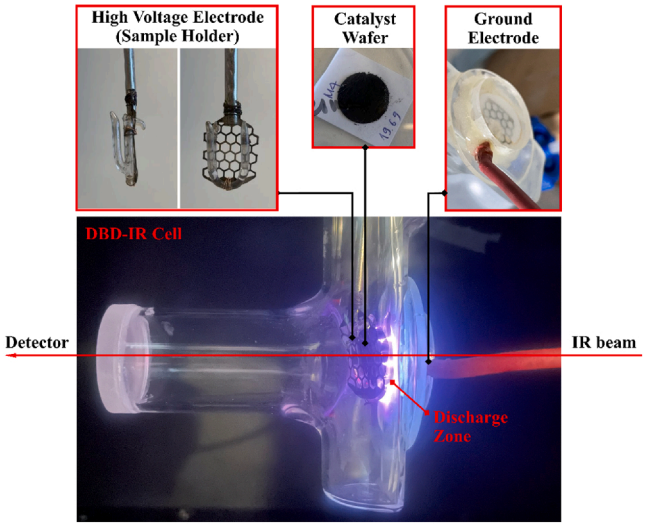

Fig. 1. DBD-*Operando* cell.

3. Results and discussion

3.1. Evaluation of Ni15Ca1 and Ni15Ba1 catalysts in thermal and plasma-assisted methanation

3.1.1. Catalytic monitoring

The catalytic performance of catalysts is reported in Fig. 2. Conventional CO_2 methanation over Ni15Ba1 was initiated at approximately 230 °C, while Ni15Ca1 and the parent 3 P-NMA became active at 300 °C (Fig. 2A). For all tested catalysts, the CO_2 conversion increased with increasing reaction temperature and reached equilibrium at 350 °C, which was lower than most published data, where the equilibrium reached at 400 °C or above. It revealed that our catalysts, whether modified with P123 (3 P-NMA) or supported with Ca and Ba, functioned significantly better. The activity sequence of our catalysts at 300 °C followed: 3 P-NMA < Ni15Ca1 < Ni15Ba. At 250 °C, the Ni15Ba1 catalyst exhibited exceptionally good activity with a CO_2 conversion of 80% and a CH_4 selectivity of 99.8%. In conventional tests, it seemed that the heavier alkaline earth metal functions better, as proposed by previous reports [12,13].

However, the performance in DBD-assisted plasma (Fig. 2B) indicated a different outcome. Ni15Ca1 was found to be the best candidate among all others, exhibiting 86.7% CO_2 conversion and nearly 100% CH_4 selectivity at 24.8 W discharge power (U_A = 23 kV). The recorded plasma temperature under these conditions was found to be about 157 °C. On the other hand, Ni15Ba1 performed poorly under the same conditions compared to the Ni15Ca1 catalyst. At 43.3 W, the CO_2 and CH_4 selectivities were 81% and 99.8%, respectively, for this catalyst. Notably, the activity of Ni15Ca1 slightly dropped after reaching a higher discharge power of 24.8 W, indicating that the adiabatic reaction occurred at a temperature of 157 °C, but this is not the case for all other catalysts. At U_A = 24 kV, the CH_4 selectivity of Ni15Ca1 was lowered to 99.9% as a result of the reverse water gas shift reaction, which produced a small amount of CO as a byproduct.

In a prior study conducted by our group [32], it was noted that Ni15/CZ displayed considerable DBD-catalytic outcomes with a similar plasma setup. Therefore, the current research employed Ni15/CZ catalyst and compared its catalytic performance with that of mixed-oxide catalysts. The results demonstrated that Ni15/CZ required a higher power consumption in order to attain the same level of activity as the

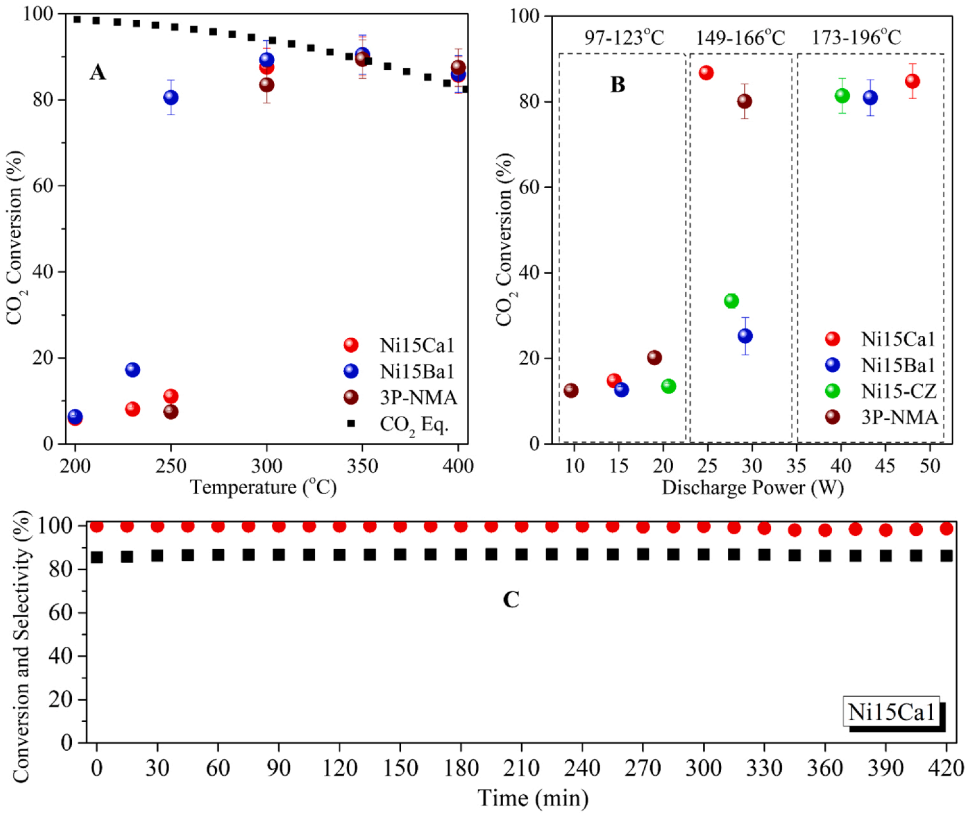

Fig. 2. Catalytic performance under A. Thermal conditions (250–450°C), B. Plasma conditions (f = 23 kHz, U_A = 22, 23, 24 kV), and C. Plasma-TOS run over Ni15Ca1 (f = 23 kHz, U_A = 23 kV) after 7 h.

mixed-oxide catalysts (Fig. 2B). Ni15Ca1 was then selected for a time-on-stream run (Fig. 2C), and the results suggested that neither CO_2 conversion nor CH_4 selectivity changed significantly after 420 min run.

Although Ni15Ba1 performed better in thermal settings, Ni15Ca1 proved to be the best catalyst system in DBD plasma conditions. In the thermal configuration, we hypothesized that the strong affinity of Ca towards CO_2 could be the reason for its low-temperature performance. To verify this hypothesis, a catalyst without Ni (Ni0Ca1) was synthesized for CO_2-TPD analysis. According to the data reported in Table 1, the total basicity of Ni0Ca1 was 216.48 μmol.g_{cat}^{-1}, which is much higher than the values found for Ni15Ba1 (ca. 136 μmol.g_{cat}^{-1}) and Ni15Ca1 (ca. 153 μmol.g_{cat}^{-1}) with a very intensive CO_2 desorption peak of strong basic sites. In this scenario, we believed that at a lower temperature (230–250 °C) when CO_2 was adsorbed, carbonate species were formed (which will be dedicated by *Operando* results in the following section), those species were strongly held by strong basic sites on the surface of Ni15Ca1 catalyst, thus hardly reacted and desorbed from the surface. The activity thereby was restricted. From 300 °C, due to the higher energy provided by heat, carbonate species were able to convert more efficiently, resulting in the better performance of the Ni15Ca1 catalyst. On the other hand, those species would indeed gain energy from highly energic electrons transferring and therefore enable the production of CH_4 through reactions with other excited species under plasma conditions. Note that the temperature recorded at this condition was 156 °C, which is much lower than in thermal conditions. Therefore, it highlighted the potential of plasma application in CO_2 methanation. In addition to that, the electrical properties of catalysts also played a significant impact on plasma performance. The measured dielectric constant, ε, on the catalysts showed that Ni15Ba1 had a value of 21.10, while the value of Ni15Ca1 was 8.87. In the case of CO_2 methanation in Plasma, we observed lower dielectric constants resulted in better catalytic performance ($\varepsilon_{3\ P\text{-}NMA}$ = 13.55 and $\varepsilon_{Ni/CZ}$ = 15.50). The reason for this could be that when working with a higher dielectric constant, not only does it increase the electric field, but it also causes local discharges to form in the voids. This limits the catalyst activation since only a small surface area is in contact with the discharge [42]. As a result, the entire discharge gap and the gas trapped in the voids [43] experience a more intense electric field [44,45]. This creates highly energetic species and hot electrons in the void spaces, which negatively impacts the catalyst performance of the catalyst, consequently.

3.1.2. *Characterizations of studied catalysts*

To provide additional insights into the behaviors of catalysts, their properties were evaluated. The characterizations of catalysts are summarized in Fig. 3 A to G, with corresponding data present in Table 1. First of all, ICP analysis indicated that the amount of Ni and M (M = Ca, Ba) were close to theoretical calculations at 15 wt% and 1 wt%, respectively (Table 1).

Fig. 3 A depicts the XRD patterns for the aforementioned catalysts. As can be seen, the diffractograms exhibited indicative reflections of a periclase-like structure of mixed oxides, as revealed by other studies [46–49]. These oxides were produced by the thermal treatment of hydrotalcite-like materials. The absence of any other reflections on the XRD diffractograms was associated with Ca and Ba being incorporated into the catalyst structure. In fact, distinguishing phases is impossible due to overlapping reflections with periclase-like MgO (JCOD 96–900–6812). Furthermore, the particle size found on reduced catalysts indicated that the Ni15Ca1 particle was at 9 nm, which was much lower than that of Ni15Ba1 (14 nm) and the parent 3 P-NMA (18 nm), cf. XRD analysis - Table 1, and TEM images - Fig. 3B. In this case, the smaller Ni^0 size of Ni15Ba1 showed a beneficial influence on the conventional CO_2 methanation.

Despite the smallest Ni^0, the strong CO_2 adsorption capacity of Ni15Ca1 limited its performance at low temperatures. The obtained CO_2-TPD profiles are shown in Fig. 3B with three broad asymmetric desorption peaks in the range of 80–600 °C. Particularly, three

Table 1
Characteristics of Ni15Ca1, Ni15Ba1, 3 P-NMA and Ni0Ca1 catalysts.

Properties	Ni15Ca1	Ni15Ba1	3 P-NMA	Ni0Ca1
Composition, wt% (ICP analysis)				
Ni	16.7	17.1	16.1	0
Mg	15.9	15.8	17.8	28.2
Al	9.2	9.3	8.5	12
M (Ca, Ba)	1.14	0.22	-	0.68
Crystalline state, Ni^0, nm (XRD analysis)				
Reduced catalysts*	9	14	18	-
Basicity, μmol·g_{cat}^{-1} (CO_2-TPD analysis)				
Total	152.8	135.9	121.1	216.6
Weak	28.28	17.59	24.44	7.92
Medium	117.74	39.55	70.4	80.34
Strong	6.28	78.74	26.13	128.3
Textural properties (Low-temperature N_2 sorption analysis)				
S_{BET}, $m^2 \cdot g^{-1}$	205.9 ± 2.1	204.6 ± 0.8	178.6 ± 1	198.5 ± 2.6
V_p, $cm^3 \cdot g^{-1}$	0.66	0.43	0.73	0.68
r_p, nm	13.33	6.47	8	18.27
Nano-Size, nm	29.14	29.33	-	30.22
Band appearance and assignments (FTIR analysis)				
3800–3300 cm^{-1}	OH groups of water bonded to M-units of hydrotalcite (i.e., Al-OH)[60–62]			
1629 cm^{-1}	The presence of neighboring water molecules in the hydrotalcite interlayer spacing[63].			
1497, 1442 cm^{-1}	Carbonate species resulted from the CO_2 adsorbed.			
1380 cm^{-1}	Carbonate species bonded to the hydroxyl surface of HT[64].			
857, 658 cm^{-1}	Appeared due to the asymmetric stretching vibrations of O-Al-O[63,65].			
445 cm^{-1}	Bonds of Al-OH in catalyst framework[63,65].			
H_2 consumption, mmol·g_{cat}^{-1} (H_2-TPR analysis)				
Total consumption	2.97	2.03	3.62	
Reduction peak at max. temperature	560 °C 0.2 670 °C 0.14 889 °C 2.62	560 °C 0.2 840 °C 1.83	450 °C 0.1 622 °C 0.06 772 °C 3.46	

*Measured from XRD analysis, 2θ = 51°

desorption peaks at 125–169 °C, 173–281 °C and 320–400 °C were attributed to the weak (surface OH), medium (acid-base Lewis pairs), and strong basic sites (low coordination surface O_2) [50,51], respectively. The strong basic site on Ni15Ca1 was slightly shifted towards higher temperature compared to 3 P-NMA and Ni15Ba1. However, it was worth noticing that all observed temperatures were lower than the data reported in the literature [52–56]. The basicity was then calculated by integrating the Gaussian desorption peaks (Table 1). It was seen that the basicity was largely dependent on the composition of brucite-like layers, the type of anions in the interlayer gaps, and the presence of Ba and Ca promoters. The total basicity of catalysts increased from 121.1 μmol.g_{cat}^{-1} to 135.9 μmol.g_{cat}^{-1} and 153.3 μmol.g_{cat}^{-1} on 3 P-NMA, Ni15Ba1, and Ni15Ca1, respectively. Herein, it was shown that the incorporation of Ca and Ba had strong effects both on the basic site distribution and the total basicity of the catalysts.

In terms of the catalyst texture, Ni15Ba1 and Ni15Ca1 showed distinct hysteresis loops (Fig. 3 C), with more porous presented on the structure of Ni15Ba1 (H_1 type) and multilayers on Ni15Ca1 (H_3 type). Both showed type IV isotherms [57–59]. The pore distribution of Ni15Ba1 fell within a narrower range. Furthermore, the incorporation of Ca and Ba led to the enhancement of the surface area (Table 1). Interestingly, despite the fact that Ba is heavier than Ca, the incorporation of both elements led to a similar surface area of 205–206 m^2/g, which is a 16% gain compared to 3 P-NMA. However, it could be seen that Ni15Ba1 had a smaller pore volume (V_p) and pore size (r_p) of 0.43 $cm^3.g^{-1}$ and 6.47 nm relative to Ni15Ca1 at 0.66 $cm^3.g^{-1}$ and 13.3 nm, respectively.

Additionally, FTIR measurements demonstrated the presence of preadsorbed carbonate species on catalysts. On both synthesized catalysts (dash lines), carbonate and preadsorbed water were predominantly observable [60–65]. However, carbonate remains stronger on Ni15Ca1 following calcination (continuous lines) than on Ni15Ba1. As noted previously in the CO_2-TPD analysis, this is the result of the Ca affinity to capture and strongly adsorbed CO_2. The assignment and band can be found in Table 1, FTIR analysis.

Lastly, the addition of Ca and Ba also altered the metal-support interactions and the reducibility of the catalysts, as revealed in Fig. 3E. Due to the reduction of nickel species, all profiles revealed two significant broad asymmetric peaks (i) between 270 °C and 520 °C ($NiO + H_2 = Ni^0 + H_2O$), and (ii) between 590 °C and 870 °C ($NiAl_2O_4 + H_2 = Ni^0 + H_2O + Al_2O_3$). The initial increase (270–340 °C) in reduction profiles was attributed to the decrease in the reductions of the isolated NiO [66] and NiO non-uniformly dispersed on the support surface. The more intense peaks that appeared at a maximum temperature of around 346–520 °C were due to a reduction in free bulk NiO/well-dispersed NiO and bulk NiO weakly interacting with the Mg(Al)O phase [67], respectively. As it could be observed with higher dominant on Ni15Ca1, suggesting that Ca supports such reduction more easily.

The highest reduction peak was observed around 722–870 °C came from nickel reduction in the NiO-MgO solid solution [68,69]. Exceptionally, a reduction peak at ca. 650–672 °C was seen on Ni15Ca1 and 3 P-NMA. This peak corresponds to the reduction of $Ni_xAl_2O_{3+x}$ [68] and has a considerable intensity on Ni15Ca1 ($Ni_xAl_2O_{3+x} + xH_2 = xNi^0 + xH_2O + Al_2O_3$). This observation indicated that Ni15Ca1 had interacted with the catalyst framework. From these results, it is possible to state that the ability of incorporating Ca into the catalyst structure is higher than that of Ba. The reduction peak was in the order of 3 P-NMA << Ni15Ca1 < Ni15Ba1. The total hydrogen consumption calculated by integrating reduction peak area (Table 1, H_2-TPR analysis) indicated a lower amount on catalysts adding 1 wt%. Ca and Ba, especially for the Ni15Ba1 catalyst (Table 1), from 3.2 mmol.g_{cat}^{-1} to 2.97 mmol.g_{cat}^{-1} and 2.03 mmol.g_{cat}^{-1}. In this case, incorporating Ba can lower catalyst reducibility, thereby performing better in conventional methanation. We emphasized that the strength of Ni-matrix interactions, represented by temperature positions, TCD intensity, and especially the H_2-consumption amount (equivalent oxygen storage capacity [70] (OSC) value), need to be assessed carefully in evaluating the reducibility of catalysts. Furthermore, in addition to the purity of the catalysts, element mapping showed that all catalysts had a homogeneous Ni-dispersion (Fig. 3 G).

Herein, for the purpose of validating the formation of intermediate species, the *Operando* was executed under both thermal and plasma conditions. Fig. 4 displays the *Operando* observations under thermal and plasma conditions, including the identification of all recorded bands [71–75].

Regarding the appearance of species under thermal conditions, it was clear that there are differences in the behaviors of Ni15Ba1 and Ni15Ca1 catalysts. Although formate species were found to be highly prominent on the surface of Ni15Ba1, carbonate species [73,76] turned out to be occupied on the surface of Ni15Ca1. It suggested that these carbonate species were formed strongly on Ni15Ca1 because of the affinity of Ca itself, as discussed in the previous section. Importantly, the absence of the carbonate band at around 1465 cm^{-1} on the Ni15Ba1 catalyst indicated that there were different ways of hydrogenating carbonate into CH_4, despite the fact that both Ni15Ca1 and Ni15Ba1 belong to the alkaline group.

Notably, the IR band at 2735 cm^{-1} paired with the IR band at 1763 cm^{-1} could be attributed to aldehyde hydrogen *HCO species (formyl) [72,73]. The appearance of the band at 1763 cm^{-1} (formyl, $HCO_{(ad)}$) during methanation suggested that the mechanism may involve formyl as an intermediate [73,77]. We believe that oxygen from M^{n+}-O^{2-} pairs (medium basic site) interacted with CO_2 to form *CO_3 species. These species would be further hydrogenated to form methane on the surface of the catalyst. The appearances of these bands differ from

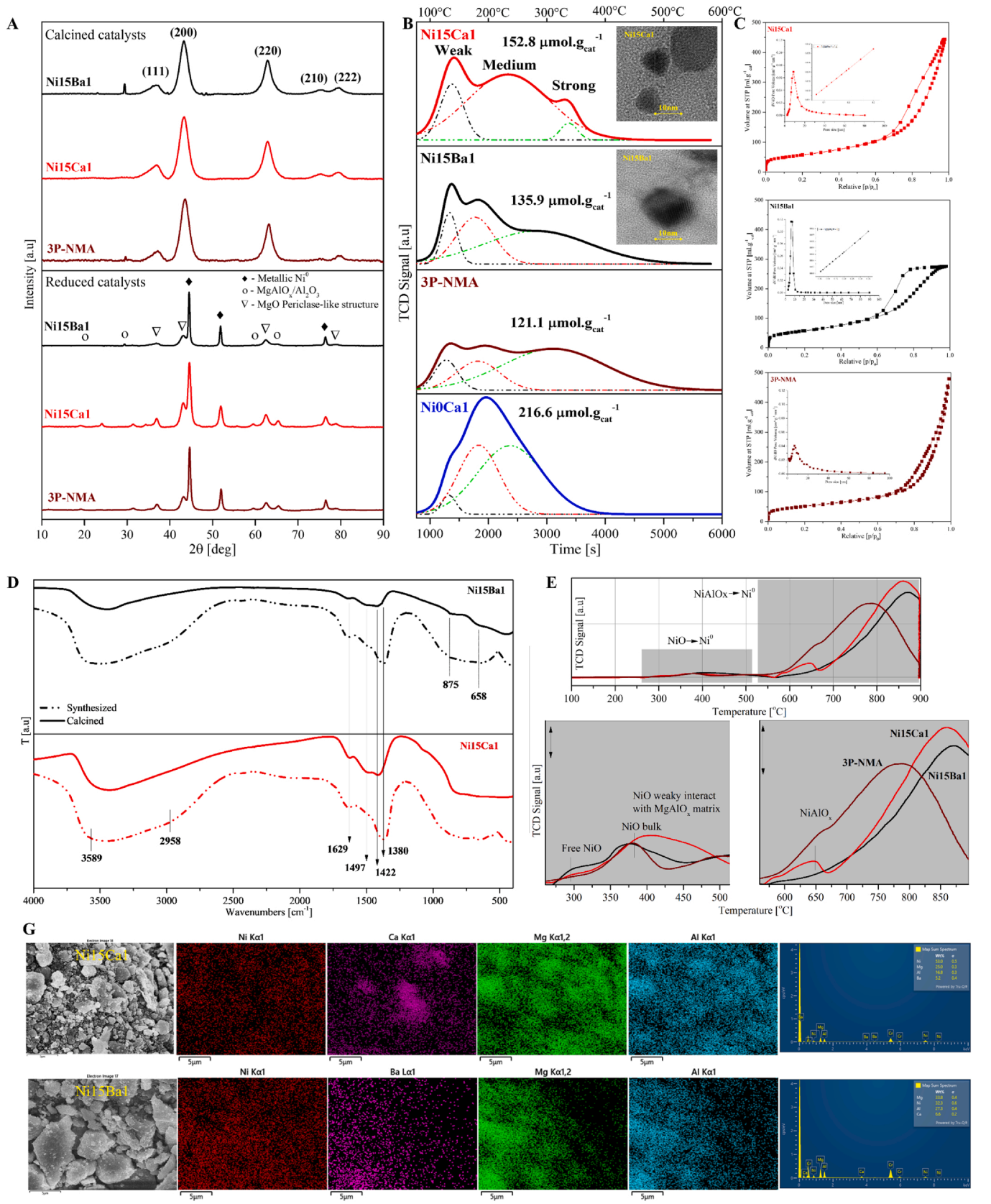

Fig. 3. Characterizations of catalysts, A. X-ray diffraction, B. CO_2-TPD profiles, C. Low-temperature N_2 sorption, D. FTIR measurements on dried and calcined samples, and E. H_2-TPR profiles. G. Elemental mapping and EDS analysis.

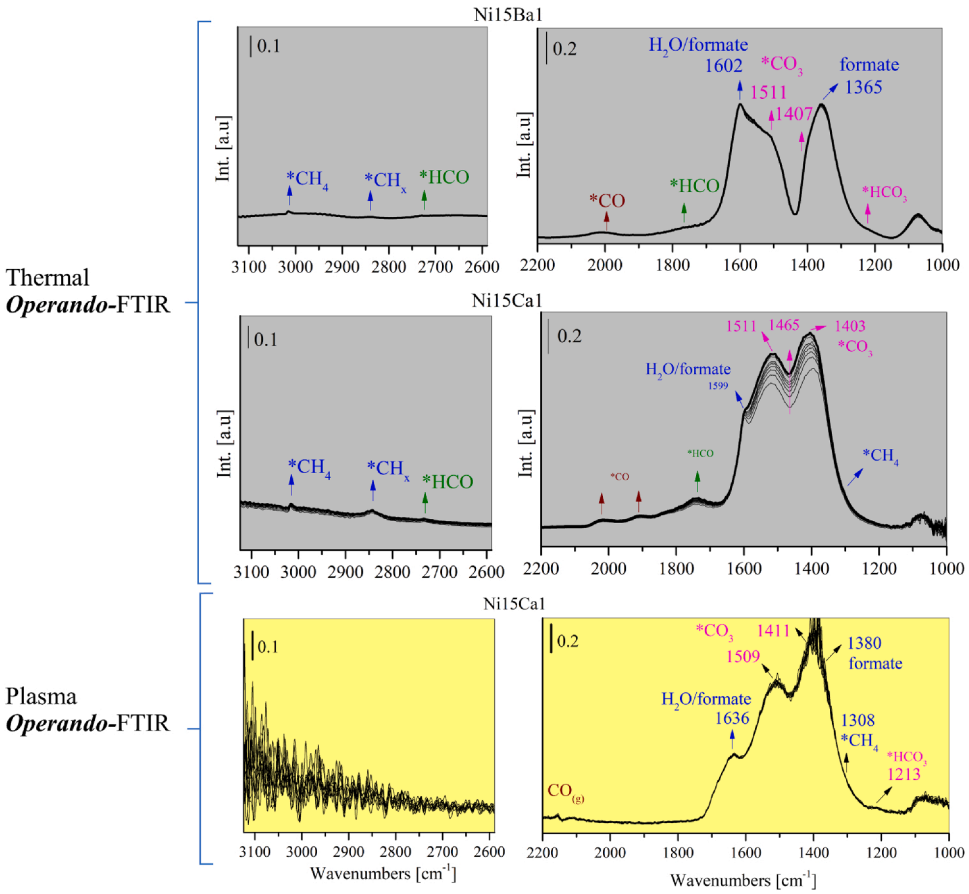

Fig. 4. *Operando* FTIR measurements in thermal and DBD plasma conditions (MS signals can be found in Supplementary Fig. 6).

Ni15Ca1 and Ni15Ba1, with higher intensity observed on Ni15Ca1. CO* species, which appeared at 2026 cm^{-1} and 1905 cm^{-1}, were more prominent on Ni15Ca1, whereas these bands were present in a wider band at 1990 cm^{-1} on Ni15Ba1. The C-H stretching vibrations of $*CH_4$ were detected at 3016 cm^{-1} [71,76], while the C-H stretching vibration of *HCOO (CHx species) was ascribed to tiny bands at 2856 cm^{-1} [71] on both catalyst surfaces. Lastly, water (*HOH species) was released as the product of CO_2 methanation was seen at 1599–1602 cm^{-1}.

In DBD-Operando measurements, the appearance of the band positions and shapes was different. As previously discussed, carbonate species were seen as dominant on the catalyst surface. However, the formate species were observed at a much higher intensity (1380 cm^{-1}). In this case, the band that appeared at 1636 cm^{-1} could be water/formate species. It could be proposed that this band corresponds to 1599–1602 cm^{-1} in thermal conditions. Furthermore, $*HCO_3$ (1213 cm^{-1}) was decreased during the reaction (discharge power at 3.7 W). We believed that $*HCO_3$ was possibly converted into a formate species via:

$$HCOOO^{-}_{(\text{hydrogen carbonate})} + H^{+} \rightarrow HCOO\text{-}OH\ (+\ H^{+}/\text{-}\ H_2O) \rightarrow HCOO^{-}_{(\text{formate})} + H_2O\cdot$$

The formate species were then hydrogenated to form $*CH_x$ and $*CH_4$. Eventually, $*CH_4$ was desorbed from the surface to receive $CH_{4(g)}$ in the gas phase as a product of the reaction.

Interestingly, neither carbonyl (*CO) nor formyl (*HCO) was detected. In this case, because of the presence of highly energic electrons, the transformation occurred very quickly, needing a lower resolution to be detected. Another point that should be highlighted is that the CO_2 methanation also occurred in the gas phase in the plasma zone, thereby passing the detection of those species on the surface. Yet, our study pointed out the clear difference between thermal and plasma. Note that the signal noise was attributed to the saturation, where all bands reached a higher level that could not be clearly distinguished by FTIR.

Based on these observations, the difference between the formation of species under thermal and plasma *Operando* measurements was drawn in Fig. 5.

Under thermal conditions, the mechanism was thought to follow: The mechanism involving formyl, therefore, could be described as follows: carbonate/hydrogen carbonate → formyl → formate → methane [29]. However, the presence of highly energic electrons in plasma configurations not only converts hydrogen carbonate (1213 cm^{-1}) into formate, which was not observed in thermal conditions but also triggers the CO_2 methanation in the gas phase, resulting in different pathways.

3.2. On the effect of wt% Ca loadings on the performance, the physical and chemical characteristics of the catalysts in the presence of plasma

Our research revealed that the incorporation of Ca at 1 wt% (Ni15Ca1) was the best catalyst in terms of plasma tests. Therefore, the influences of various Ca concentrations need to be investigated. This section was carried out to examine the impact of different Ca loadings (0.5, 1, 2, 3, 5 wt%) on DBD plasma catalytic performance.

The results are depicted in Fig. 6, in which one can be observed was that, with the exception of Ni15Ca1, the activity increased as the applied voltage U_A increased from 22 to 24 kV. The CH_4 recorded selectivity for all catalysts ranged from 99.5% to 99.7%. Catalysts containing 3 wt%. Ca showed 78% CO_2 conversion and 99.7% CH_4 selectivity at 24 kV also appeared as a good candidate. However, in terms of power usage, Ni15Ca5 showed a better result in converting ca. 65% of CO_2 at ca. 28 W (Fig. 6A).

In order to understand the electrical properties further, the capacitance was then calculated on the basis of the Lissajous figures (Lissajous

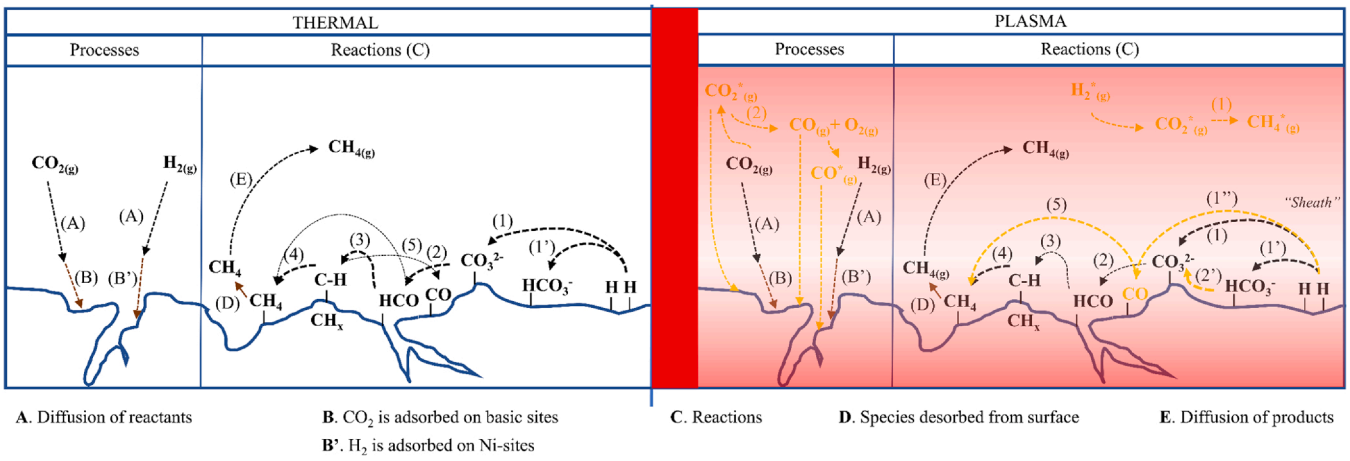

Fig. 5. *Operando* thermal and plasma observations.

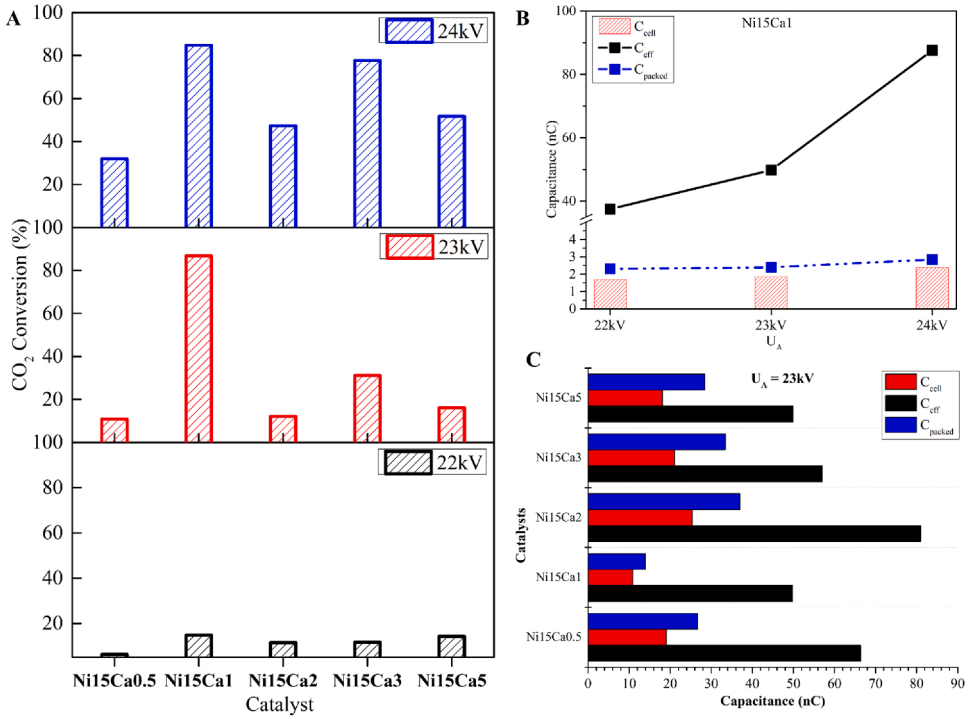

Fig. 6. A. Plasma behaviors of Ni15Cax series (x = 0.5, 1, 2, 3, 5), B. calculated capacitance of Ni15Ca1, and C. Measured capacitance at U_A = 23 kV for all catalysts.

figures of Ni15Cax catalyst series are present in Supplementary Fig. 7). On Ni15Ca1, the effective capacitance (C_{eff}) improved significantly from U_A = 23–24 kV. The plasma temperature recorded during these trials suggested a rise from approximately 150 °C to 195 °C. In this scenario, the C_{eff} seemed to be more sensitive to temperature than C_{packed} and C_{cell} (Fig. 6B). In other words, raising the power significantly impacts the effective capacitance before affecting C_{packed}. The change in C_{cell} was the result of C_{eff} and C_{packed} alterations. On the other hand, the activity of Ni15Ca1 decreased slightly at 24 kV, leading us to assume that the C_{eff} has a modestly favorable effect on plasma behavior. Capacitance calculations for all catalysts were reported in Fig. 6C. According to the results, the lowest C_{packed} was observed in Ni15Ca1. Assuming that the packed region contains catalysts and gas, and the gas capacitance varies within a narrow range, it is possible to claim that catalysts with a lower dielectric constant will perform better. The higher the effective capacitance, the better the catalytic results. However, this is only true for a certain level of C_{eff}; higher than that, the catalyst performance would be negatively affected.

Fig. 7 shows the relationship between discharge power, specific energy input, and energy efficiency for the studied catalysts as a function of Ca loading.

In Fig. 7, with a discharge power of 20 W, the system received energy (η) primarily for molecular vibration [78] as indicated by the low SEI (below 2.1 eV/molecule); as a result, low efficiency was seen. When this threshold was surpassed, however, the energy efficiency increased by more than 60% over Ni15Ca1 catalysts, while the other energy efficiency values were rather poorer. In particular, the η value for Ni15Ca1 was found to be 73.2%, which, to the best of our knowledge, is the highest value reported in the literature.

4. Conclusions

In this study, calcium and barium were introduced to the 3 P-NMA catalyst system to avoid CO_2 methanation limitations. The results

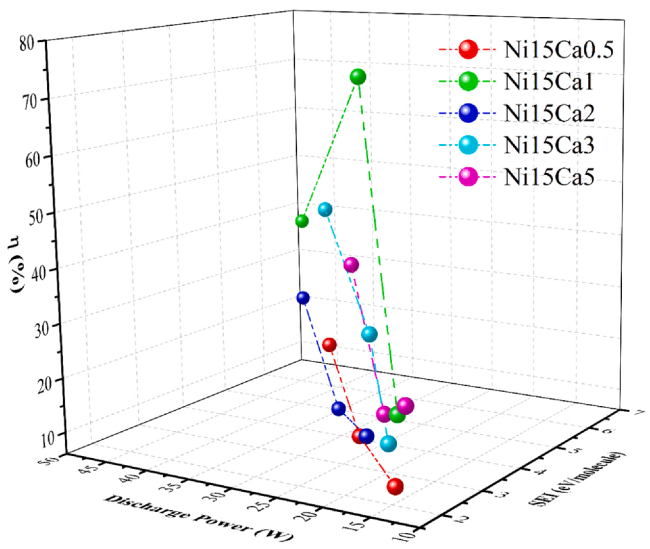

Fig. 7. Discharge power (W), specific energy input (eV/molecule) versus energy efficiency (%).

demonstrated that Ni15Ca1 could achieve a CO_2 conversion of approximately 87% and a CH_4 selectivity of 100% at a power of 24.8 W (156°C). The energy efficiency obtained was the highest value reported in the literature. Ni15Ba1 was found to be effective for conventional methanation at low temperatures. In such a case, calcium addition leads to a strong absorption of CO_2, thereby limiting its activity under mild conditions. However, because of the presence of energetic electrons and excited species in the plasma, collisions between such species favor the reaction and transformation of carbonates into products more efficiently on the Ni15Ca1 catalyst. The addition of Ca with various loadings revealed that the highest activity with the lowest discharge power was achieved at a concentration of 1 wt%. Ca.

Furthermore, the addition of Ca and Ba altered the nature of the catalysts, redistributed the basic sites, and increased the reducibility. It was also observed that Ca appeared to interact more with the matrix than the Ba element. Overall, adding Ca and Ba led to the enhancement of CO_2 methanation catalytic activity. This improvement is typically attributed to increased dispersion of active metals, and an increase in the alkalinity of the support, all of which greatly enhance the initial chemisorption and activation of CO_2. The different thermal and plasma performance behavior was also explained via *Operando* studies in which formyl (HCO^-) appeared to be intermediate in thermal methanation. The participation of hydrogencarbonate (HCO_3^-), on the other hand, was evidenced in DBD-plasma conditions.

CRediT authorship contribution statement

Minh NGUYEN QUANG: Conceptualization, Methodology, Investigation, Data Curation, Writing Original Draft, Writing Review and Editing, Visualization; **Federico AZZOLINA JURY**: Conceptualization, Methodology, Validation, Formal analysis, Investigation, Resources, Data Curation, Writing Original Draft, Writing Review and Editing, Visualization, Supervision, Project administration, funding acquisition; **Bogdan SAMOJEDEN**: Conceptualization, Methodology, Validation, Formal analysis, Investigation, Resources, Data Curation, Writing Review and Editing, Visualization, Supervision, funding acquisition; **Monika MOTAK**: Conceptualization, Methodology, Validation, Formal analysis, Investigation, Resources, Data Curation, Writing Review and Editing, Visualization, Supervision, funding acquisition; **Patrick DA COSTA**: Conceptualization, Methodology, Validation, Formal analysis, Investigation, Resources, Data Curation, Writing Original Draft, Writing Review and Editing, Visualization, Supervision, Project administration, funding acquisition.

Declaration of Competing Interest

The authors declare that they have no known competing financial interests or personal relationships that could have appeared to influence the work reported in this paper.

Data availability

Data will be made available on request.

Acknowledgments

This work has received support from the European Research Framework Program: H2020 | Marie Skłodowska-Curie Action (MSCA), PIONEER project: plasma catalysis for CO_2 recycling (Grant no. 813393). The authors would like to thank Professor Sylvain Marinel (sylvain.marinel@ensicaen.fr), CNRS, Caen, for the help with dielectric constant measurements. Monika Motak's research was partially supported by program "Excellence initiative – research university" for the AGH University of Science and Technology. Bogdan Samojeden acknowledges the financial support of Grant AGH 16.16.210.476.

Appendix A. Supporting information

Supplementary data associated with this article can be found in the online version at doi:10.1016/j.apcatb.2023.122952.

References

[1] B.E.s.I.S. Research, Temperature Change vs. Carbon Dioxide Concentration, Berkeley Earth, (2022). https://berkeleyearth.org/dv/temperature-change-vs-carbon-dioxide-concentration/.
[2] P. Gabrielli, M. Gazzani, M. Mazzotti, The role of carbon capture and utilization, carbon capture and storage, and biomass to enable a Net-Zero-CO_2 emissions chemical industry, Ind. Eng. Chem. Res. 59 (2020) 7033–7045, https://doi.org/10.1021/acs.iecr.9b06579.
[3] IEA, Carbon capture, utilisation and storage. https://www.iea.org/fuels-and-technologies/carbon-capture-utilisation-and-storage.
[4] M. Götz, J. Lefebvre, F. Mörs, A. McDaniel Koch, F. Graf, S. Bajohr, R. Reimert, T. Kolb, Renewable power-to-gas: A technological and economic review, Renew. Energy 85 (2016) 1371–1390, https://doi.org/10.1016/j.renene.2015.07.066.
[5] M. Götz, A. Koch, F. Graf, State of the Art and Perspectives of CO2 Methanation Process Concepts for Power-to-Gas Applications, International Gas Research Conference Proceedings, 1 (2014). https://www.researchgate.net/publication/273139805_State_of_the_Art_and_Perspectives_of_CO2_Methanation_Process_Concepts_for_Power-to-Gas_Applications.
[6] W. Wei, G. Jinlong, Methanation of carbon dioxide: an overview, Front. Chem. Sci. Eng. 5 (2011) 2–10, https://doi.org/10.1007/s11705-010-0528-3.
[7] M.A.A. Aziz, A.A. Jalil, S. Triwahyono, A. Ahmad, CO_2 methanation over heterogeneous catalysts: recent progress and future prospects, Green. Chem. 17 (2015) 2647–2663, https://doi.org/10.1039/C5GC00119F.
[8] W.J. Lee, C. Li, H. Prajitno, J. Yoo, J. Patel, Y. Yang, S. Lim, Recent trend in thermal catalytic low temperature CO_2 methanation: A critical review, Catal. Today 368 (2021) 2–19, https://doi.org/10.1016/j.cattod.2020.02.017.
[9] C. Lv, L. Xu, M. Chen, Y. Cui, X. Wen, Y. Li, B. C.-e. Wu, Z. Yang, X. Miao, Q. Hu, Shou, Recent progresses in constructing the highly efficient Ni based catalysts with advanced low-temperature activity toward CO_2 methanation, Front. Chem. 8 (2020), https://doi.org/10.3389/fchem.2020.00269.
[10] K. Liu, X. Xu, J. Xu, X. Fang, L. Liu, X. Wang, The distributions of alkaline earth metal oxides and their promotional effects on Ni/CeO_2 for CO_2 methanation, J. CO_2 Util. 38 (2020) 113–124, https://doi.org/10.1016/j.jcou.2020.01.016.
[11] I.V. Yentekakis, P. Vernoux, G. Goula, A. Caravaca, Electropositive promotion by alkalis or alkaline earths of Pt-group metals in emissions control catalysis: a status report, Catalysts 9 (2019) 157, https://doi.org/10.3390/catal9020157.
[12] M. Guo, G. Lu, The difference of roles of alkaline-earth metal oxides on silica-supported nickel catalysts for CO_2 methanation, RSC Adv. 4 (2014) 58171–58177, https://doi.org/10.1039/C4RA06202G.
[13] C. Liang, X. Hu, T. Wei, P. Jia, Z. Zhang, D. Dong, S. Zhang, Q. Liu, G. Hu, Methanation of CO_2 over Ni/Al_2O_3 modified with alkaline earth metals: Impacts of oxygen vacancies on catalytic activity, Int. J. Hydrog. Energy 44 (2019) 8197–8213, https://doi.org/10.1016/j.ijhydene.2019.02.014.
[14] Q. Pan, J. Peng, T. Sun, S. Wang, S. Wang, Insight into the reaction route of CO_2 methanation: Promotion effect of medium basic sites, Catal. Commun. 45 (2014) 74–78, https://doi.org/10.1016/j.catcom.2013.10.034.

[15] Y. Feng, W. Yang, W. Chu, Effect of Ca modification on the catalytic performance of Ni/AC for CO_2 methanation, Integr. Ferroelectr. 172 (2016) 40–48, https://doi.org/10.1080/10584587.2016.1175333.

[16] L. Xu, H. Yang, M. Chen, F. Wang, D. Nie, L. Qi, X. Lian, H. Chen, M. Wu, CO_2 methanation over Ca doped ordered mesoporous Ni-Al composite oxide catalysts: The promoting effect of basic modifier, J. CO_2 Util. 21 (2017) 200–210, https://doi.org/10.1016/j.jcou.2017.07.014.

[17] C. Liang, Z. Ye, D. Dong, S. Zhang, Q. Liu, G. Chen, C. Li, Y. Wang, X. Hu, Methanation of CO_2: Impacts of modifying nickel catalysts with variable-valence additives on reaction mechanism, Fuel 254 (2019), 115654, https://doi.org/10.1016/j.fuel.2019.115654.

[18] A. Vaccari, Preparation and catalytic properties of cationic and anionic clays, Catal. Today 41 (1998) 53–71, https://doi.org/10.1016/S0920-5861(98)00038-8.

[19] T. Zhao, X. Hu, Y. Wu, Z. Zhang, Hydrogenation of CO_2 to formate with H_2: transition metal free catalyst based on a lewis pair, Angew. Chem. Int. Ed. 58 (2019) 722–726, https://doi.org/10.1002/anie.201809634.

[20] D. Mei, X. Tu, Atmospheric pressure non-thermal plasma activation of CO_2 in a packed-bed dielectric barrier discharge reactor, ChemPhysChem 18 (2017) 3253–3259, https://doi.org/10.1002/cphc.201700752.

[21] R. Benrabbah, C. Cavaniol, H. Liu, S. Ognier, S. Cavadias, M.E. Gálvez, P. Da Costa, Plasma DBD activated ceria-zirconia-promoted Ni-catalysts for plasma catalytic CO_2 hydrogenation at low temperature, Catal. Commun. 89 (2017) 73–76, https://doi.org/10.1016/j.catcom.2016.10.028.

[22] M.C. Bacariza, M. Biset-Peiró, I. Graça, J. Guilera, J. Morante, J.M. Lopes, T. Andreu, C. Henriques, DBD plasma-assisted CO_2 methanation using zeolite-based catalysts: Structure composition-reactivity approach and effect of Ce as promoter, J. CO_2 Util. 26 (2018) 202–211, https://doi.org/10.1016/j.jcou.2018.05.013.

[23] J. Li, C. Ma, S. Zhu, F. Yu, B. Dai, D. Yang, A review of recent advances of dielectric barrier discharge plasma in catalysis, Nanomaterials 9 (2019) 1428, https://doi.org/10.3390/nano9101428.

[24] Z. Fan, K. Sun, N. Rui, B. Zhao, C.-j. Liu, Improved activity of Ni/$MgAl_2O_4$ for CO_2 methanation by the plasma decomposition, J. Energy Chem. 24 (2015) 655–659, https://doi.org/10.1016/j.jechem.2015.09.004.

[25] R. Dębek, F. Azzolina-Jury, A. Travert, F. Maugé, A review on plasma-catalytic methanation of carbon dioxide – Looking for an efficient catalyst, Renew. Sustain. Energy Rev. 116 (2019), 109427, https://doi.org/10.1016/j.rser.2019.109427.

[26] M. Nizio, R. Benrabbah, M. Krzak, R. Debek, M. Motak, S. Cavadias, M.E. Gálvez, P. Da Costa, Low temperature hybrid plasma-catalytic methanation over Ni-Ce-Zr hydrotalcite-derived catalysts, Catal. Commun. 83 (2016) 14–17, https://doi.org/10.1016/j.catcom.2016.04.023.

[27] H. Puliyalil, D. Lašič Jurković, V. Dasireddy, B. Likozar, A review of plasma-assisted catalytic conversion of gaseous carbon dioxide and methane into value-added platform chemicals and fuels, RSC Adv. 48 (2018) 27481–27508, https://doi.org/10.1039/C8RA03146K.

[28] A. Bogaerts, G. Centi, Plasma technology for CO_2 conversion: a personal perspective on prospects and gaps, Front. Energy Res. 8 (2020) 111, https://doi.org/10.3389/fenrg.2020.00111.

[29] M. Nguyen-Quang, F. Azzolina-Jury, F. Thibault-Starzyk, A. Travert, M. Ziąbka, B. Samojeden, M. Motak, P. Da Costa, Unveiling the potential of surfactant Pluronic-P123 application during the synthesis of Ni-hydrotalcite-derived catalysts for low-temperature CO_2 methanation: A novel approach, Appl. Mater. Today 32 (2023), 101805, https://doi.org/10.1016/j.apmt.2023.101805.

[30] M. Nguyen-Quang, F. Azzolina-Jury, B. Samojeden, M. Motak, P. Da Costa, On the influence of the preparation routes of NiMgAl-mixed oxides derived from hydrotalcite on their CO_2 methanation catalytic activities, Int. J. Hydrog. Energy 47 (2022) 37783–37791, https://doi.org/10.1016/j.ijhydene.2022.08.278.

[31] X. Zheng, Z. Song, E. Liu, Y. Zhang, Z. Li, Preparation of phosphoric acid-functionalized SBA-15 and its high efficient selective adsorption separation of lanthanum ions, J. Chem. Eng. Data 65 (2020) 746–756, https://doi.org/10.1021/acs.jced.9b00976.

[32] M. Mikhail, P.D. Costa, J. Amouroux, S. Cavadias, M. Tatoulian, S. Ognier, M. E. Gálvez, Effect of Na and K impurities on the performance of Ni/CeZrOx catalysts in DBD plasma-catalytic CO_2 methanation, Fuel 306 (2021), 121639, https://doi.org/10.1016/j.fuel.2021.121639.

[33] J.K. Lefkowitz, M. Uddi, B.C. Windom, G. Lou, Y. Ju, In situ species diagnostics and kinetic study of plasma activated ethylene dissociation and oxidation in a low temperature flow reactor, Proc. Combust. Inst. 35 (2015) 3505–3512, https://doi.org/10.1016/j.proci.2014.08.001.

[34] M. Rivallan, E. Fourré, S. Aiello, J.-M. Tatibouët, F. Thibault-Starzyk, Insights into the mechanisms of isopropanol conversion on γ-Al_2O_3 by dielectric barrier discharge, Plasma Process. Polym. 9 (2012) 850–854, https://doi.org/10.1002/ppap.201200021.

[35] B. Eliasson, U. Kogelschatz, B. Xue, L.M. Zhou, Hydrogenation of carbon dioxide to methanol with a discharge-activated catalyst, Ind. Eng. Chem. Res. 37 (1998) 3350–3357, https://doi.org/10.1021/ie9709401.

[36] K.P. Francke, R. Rudolph, H. Miessner, Design and operating characteristics of a simple and reliable DBD reactor for use with atmospheric air, Plasma Chem. Plasma Process. 23 (2003) 47–57, https://doi.org/10.1023/A:1022412718224.

[37] R. Valdivia-Barrientos, J. Pacheco-Sotelo, M. Pacheco-Pacheco, J.S. Benítez-Read, R. López-Callejas, Analysis and electrical modelling of a cylindrical DBD configuration at different operating frequencies, Plasma Sources Sci. Technol. 15 (2006) 237–245, https://doi.org/10.1088/0963-0252/15/2/008.

[38] T.C. Manley, The electric characteristics of the ozonator discharge, Trans. Electrochem. Soc. 84 (1943) 83, https://doi.org/10.1149/1.3071556.

[39] T. Butterworth, R. Elder, R. Allen, Effects of particle size on CO_2 reduction and discharge characteristics in a packed bed plasma reactor, Chem. Eng. J. 293 (2016) 55–67, https://doi.org/10.1016/j.cej.2016.02.047.

[40] F. Azzolina Jury, I. Polaert, L. Estel, L.B. Pierella, Synthesis and characterization of MEL and FAU zeolites doped with transition metals for their application to the fine chemistry under microwave irradiation, Appl. Catal. A: Gen. 453 (2013) 92–101, https://doi.org/10.1016/j.apcata.2012.11.046.

[41] X. Tu, J. Whitehead, T. Nozaki, Plasma catalysis fundamentals and applications, Fundam. Appl. (2019), https://doi.org/10.1007/978-3-030-05189-1.

[42] W. Wang, H.-H. Kim, K. Van Laer, A. Bogaerts, Streamer propagation in a packed bed plasma reactor for plasma catalysis applications, Chem. Eng. J. 334 (2018) 2467–2479, https://doi.org/10.1016/j.cej.2017.11.139.

[43] D. Ray, C. Subrahmanyam, CO_2 decomposition in a packed DBD plasma reactor: influence of packing materials, RSC Adv. 6 (2016) 39492–39499, https://doi.org/10.1039/C5RA27085E.

[44] K. Van Laer, A. Bogaerts, Influence of gap size and dielectric constant of the packing material on the plasma behaviour in a packed bed DBD reactor: a fluid modelling study, Plasma Process. Polym. 14 (2017) 1600129, https://doi.org/10.1002/ppap.201600129.

[45] K. Van Laer, A. Bogaerts, How bead size and dielectric constant affect the plasma behaviour in a packed bed plasma reactor: a modelling study, Plasma Sources Sci. Technol. 26 (2017), 085007, https://doi.org/10.1088/1361-6595/aa7c59.

[46] C. Forano, U. Costantino, V. Prévot, C.T. Gueho, Chapter 14.1 - Layered Double Hydroxides (LDH), Dev. Clay Sci. 5 (2013) 745–782, https://doi.org/10.1016/B978-0-08-098258-8.00025-0.

[47] K. Świrk, M. Motak, T. Grzybek, M. Rønning, P. Da Costa, Effect of low loading of yttrium on Ni-based layered double hydroxides in CO_2 reforming of CH_4, React. Kinet., Mech. Catal. 126 (2019) 611–628, https://doi.org/10.1007/s11144-018-1515-9.

[48] K. Świrk, M.E. Gálvez, M. Motak, T. Grzybek, M. Rønning, P. Da Costa, Dry reforming of methane over Zr- and Y-modified Ni/Mg/Al double-layered hydroxides, Catal. Commun. 117 (2018) 26–32, https://doi.org/10.1016/j.catcom.2018.08.024.

[49] O.D. Pavel, D. Tichit, I.-C. Marcu, Acido-basic and catalytic properties of transition-metal containing Mg–Al hydrotalcites and their corresponding mixed oxides, Appl. Clay Sci. 61 (2012) 52–58, https://doi.org/10.1016/j.clay.2012.03.006.

[50] F. Prinetto, G. Ghiotti, R. Durand, D. Tichit, Investigation of acid−base properties of catalysts obtained from layered double hydroxides, J. Phys. Chem. B 104 (2000) 11117–11126, https://doi.org/10.1021/jp002715u.

[51] J.C. Lavalley, Infrared spectrometric studies of the surface basicity of metal oxides and zeolites using adsorbed probe molecules, Catal. Today 27 (1996) 377–401, https://doi.org/10.1016/0920-5861(95)00161-1.

[52] D.Y. Kalai, K. Stangeland, H. Li, Z. Yu, The effect of La on the hydrotalcite derived Ni catalysts for dry reforming of methane, Energy Procedia 142 (2017) 3721–3726, https://doi.org/10.1016/j.egypro.2017.12.267.

[53] R. Dębek, M. Radlik, M. Motak, M.E. Galvez, W. Turek, P. Da Costa, T. Grzybek, Ni-containing Ce-promoted hydrotalcite derived materials as catalysts for methane reforming with carbon dioxide at low temperature – On the effect of basicity, Catal. Today 257 (2015) 59–65, https://doi.org/10.1016/j.cattod.2015.03.017.

[54] D. Wierzbicki, R. Baran, R. Dębek, M. Motak, M.E. Gálvez, T. Grzybek, P. Da Costa, P. Glatzel, Examination of the influence of La promotion on Ni state in hydrotalcite-derived catalysts under CO_2 methanation reaction conditions: Operando X-ray absorption and emission spectroscopy investigation, Appl. Catal. B Environ. 232 (2018) 409–419, https://doi.org/10.1016/j.apcatb.2018.03.089.

[55] A. Corma, V. Fornés, R.M. Martín-Aranda, F. Rey, Determination of base properties of hydrotalcites: Condensation of benzaldehyde with ethyl acetoacetate, J. Catal. 134 (1992) 58–65, https://doi.org/10.1016/0021-9517(92)90209-Z.

[56] F. Prinetto, G. Ghiotti, P. Graffin, D. Tichit, Synthesis and characterization of sol–gel Mg/Al and Ni/Al layered double hydroxides and comparison with co-precipitated samples, Microporous Mesoporous Mater. 39 (2000) 229–247, https://doi.org/10.1016/S1387-1811(00)00197-9.

[57] D. Wierzbicki, M. Motak, T. Grzybek, M.E. Gálvez, P. Da Costa, The influence of lanthanum incorporation method on the performance of nickel-containing hydrotalcite-derived catalysts in CO_2 methanation reaction, Catal. Today 307 (2018) 205–211, https://doi.org/10.1016/j.cattod.2017.04.020.

[58] F. Cavani, F. Trifiró, A.J.C.T. Vaccari, Hydrotalcite-type anionic clays: Preparation, properties and applications 11 (1991) 173–301, https://doi.org/10.1016/0920-5861(91)80068-K.

[59] A. Rodrigues, C. Henriques, J. Monteiro, Influence of Ni content on physico-chemical characteristics of Ni, Mg, Al-Hydrotalcite like compounds, Mater. Res. 6 (2003) 563–568, https://doi.org/10.1590/S1516-14392003000400024.

[60] A. Obadiah, R. Kannan, P. Ravichandiran, A. Ramasubbu, S. Kumar, Nano hydrotalcite as a novel catalyst for biodiesel conversion, Digest Journal of Nanomaterials and Biostructures, 7 (2012) 321–327. https://www.researchgate.net/publication/228073178_Nano_hydrotalcite_as_a_novel_catalyst_for_biodiesel_conversion.

[61] E.Heraldy Heriyanto, K.D. Nugrahaningtyas, X-RAY diffraction and fourier transform infrared study of Ca-Mg-Al hydrotalcite from artificial brine water with synthesis hydrothermal treatments, IOP Conf. Ser. Mater. Sci. Eng. 333 (2018), 012006, https://doi.org/10.1088/1757-899X/333/1/012006.

[62] S. Kannan, D. Kishore, K. Hadjiivanov, H. Knözinger, FTIR study of low-temperature CO adsorption on MgAl-hydrotalcite and its calcined forms, Langmuir 19 (2003) 5742–5747, https://doi.org/10.1021/la030019q.

[63] B. Wiyantoko, P. Kurniawati, T.E. Purbaningtias, I. Fatimah, Synthesis and characterization of hydrotalcite at different Mg/Al molar ratios, Procedia Chem. 17 (2015) 21–26, https://doi.org/10.1016/j.proche.2015.12.115.

[64] P. Parashar, V. Sharma, D.D. Agarwal, N. Richhariya, Rapid synthesis of hydrotalcite with high antacid activity, Mater. Lett. 74 (2012) 93–95, https://doi.org/10.1016/j.matlet.2011.12.115.
[65] M. del Arco, C. Martin, I. Martin, V. Rives, R. Trujillano, A FTIR spectroscopic study of surface acidity and basicity of mixed Mg, Al-oxides obtained by thermal decomposition of hydrotalcite, Spectrochim. Acta Part A: Mol. Spectrosc. 49 (1993) 1575–1582, https://doi.org/10.1016/0584-8539(93)80114-P.
[66] O.W. Perez-Lopez, A. Senger, N.R. Marcilio, M.A. Lansarin, Effect of composition and thermal pretreatment on properties of Ni–Mg–Al catalysts for CO_2 reforming of methane, Appl. Catal. A: Gen. 303 (2006) 234–244, https://doi.org/10.1016/j.apcata.2006.02.024.
[67] D. Tichit, F. Medina, B. Coq, R. Dutartre, Activation under oxidizing and reducing atmospheres of Ni-containing layered double hydroxides, Appl. Catal. A: Gen. 159 (1997) 241–258, https://doi.org/10.1016/S0926-860X(97)00085-9.
[68] N. Ichikuni, D. Murata, S. Shimazu, T. Uematsu, Promoting effect of $NiAl_2O_4$ for supported Ni particles on sprayed Ni/Al_2O_3 catalysts, Catal. Lett. 69 (2000) 33–36, https://doi.org/10.1023/A:1019009620601.
[69] D. Hu, J. Gao, Y. Ping, L. Jia, P. Gunawan, Z. Zhong, G. Xu, F. Gu, F. Su, Enhanced investigation of CO methanation over Ni/Al_2O_3 catalysts for synthetic natural gas production, Ind. Eng. Chem. Res. 51 (2012) 4875–4886, https://doi.org/10.1021/ie300049f.
[70] G. Botzolaki, G. Goula, A. Rontogianni, E. Nikolaraki, N. Chalmpes, P. Zygouri, M. Karakassides, D. Gournis, N. Charisiou, M. Goula, S. Papadopoulos, I. Yentekakis, CO_2 methanation on supported rh nanoparticles: the combined effect of support oxygen storage capacity and Rh particle size, Catalysts 10 (2020) 944, https://doi.org/10.3390/catal10080944.
[71] K. Ito, H. Bernstein, The vibrational spectra of the formate, acetate, and oxalate ions, Can. J. Chem. 34 (2011) 170–178, https://doi.org/10.1139/v56-021.
[72] J. Raskó, J. Kiss, Adsorption and surface reactions of acetaldehyde on alumina-supported noble metal catalysts, Catal. Lett. 101 (2005) 71–77, https://doi.org/10.1007/s10562-004-3752-y.
[73] B. Miao, S.S.K. Ma, X. Wang, H. Su, S.H. Chan, Catalysis mechanisms of CO_2 and CO methanation, Catal. Sci. Technol. 6 (2016) 4048–4058, https://doi.org/10.1039/C6CY00478D.
[74] H.L. Huynh, J. Zhu, G. Zhang, Y. Shen, W.M. Tucho, Y. Ding, Z. Yu, Promoting effect of Fe on supported Ni catalysts in CO_2 methanation by in situ DRIFTS and DFT study, J. Catal. 392 (2020) 266–277, https://doi.org/10.1016/j.jcat.2020.10.018.
[75] K. Hadjiivanov, Chapter Two - Identification and characterization of surface hydroxyl groups by infrared spectroscopy, Adv. Catal. 57 (2014) 99–318, https://doi.org/10.1016/B978-0-12-800127-1.00002-3.
[76] P. Völs, S. Hilbert, B. Störr, N. Bette, A. Lißner, J. Seidel, F. Mertens, Methanation of CO_2 and CO by (Ni,Mg,Al)-hydrotalcite-derived and related catalysts with varied magnesium and aluminum oxide contents, Ind. Eng. Chem. Res. 60 (2021) 5114–5123, https://doi.org/10.1021/acs.iecr.1c00028.
[77] S. Akamaru, T. Shimazaki, M. Kubo, T. Abe, Density functional theory analysis of methanation reaction of CO_2 on Ru nanoparticle supported on TiO_2 (101), Appl. Catal. A Gen. 470 (2014) 405–411, https://doi.org/10.1016/j.apcata.2013.11.016.
[78] S. Li, M. Ongis, G. Manzolini, F. Gallucci, Non-thermal plasma-assisted capture and conversion of CO_2, Chem. Eng. J. 410 (2021), 128335, https://doi.org/10.1016/j.cej.2020.128335.